Journal of Cleaner Production 456 (2024) 142317

Contents lists available at ScienceDirect

Journal of Cleaner Production

journal homepage: www.elsevier.com/locate/jclepro

Investigation of gold adsorption by ironbark biochar using response surface methodology and artificial neural network modelling

Mahmuda Akter Mele [a], Ravinder Kumar [a], Tewodros Kassa Dada [a], Amir Heydari [b], Elsa Antunes [a,*]

[a] College of Science and Engineering, James Cook University, Townsville, QLD, 4811, Australia
[b] Chemical Engineering Group, Faculty of Engineering, University of Mohaghegh Ardabili, Ardabil, Iran

ARTICLE INFO

Handling editor: Zhifu Mi

Keywords:
Biochar
Adsorption
Response surface methodology
Artificial neural network
Ironbark
Gold removal

ABSTRACT

Due to the importance and economic value of gold in various applications, recovering gold from waste streams like tailings and industrial wastewater is essential. Biochar with a high surface area and porosity is considered a potential low-cost adsorbent for gold reclaiming from aqueous media. Therefore, this study aims to develop a high-quality biochar with excellent physicochemical properties to efficiently remove gold from aqueous media. To accomplish this, biochar was obtained from pyrolysis of ironbark (IB) biomass at 500 °C which has a surface area of 493.79 m^2/g. Subsequently, the biochar was investigated for adsorption of gold from aqueous media, which exhibited a maximum adsorption capacity of 858 mg/g. Isotherm results showed that the adsorption of gold by biochar followed the Langmuir model, indicating monolayer adsorption. Further, response surface methodology (RSM) and an artificial neural network (ANN) combined with the Salp Swarm Algorithm (SSA) were used to analyze the generated results (ANN-SSA). The RSM prediction model fit was adequate ($R^2 = 0.99$). However, comparing the statistical data revealed that ANN-SSA outperformed RSM in predicting experimental results. Overall, this study suggested that biochar derived from IB biomass could be used as a potential adsorbent to recover gold from an aqueous solution. This article presents a unique and innovative study on the utilization of ironbark biochar for the purpose of gold adsorption.

1. Introduction

Gold is a valuable metal which has a high commercial value throughout the world. Gold has distinctive physical, chemical, and optical properties, and has been commonly utilized in catalysis (Carabineiro, 2019), biomedical applications (Bansal et al., 2020), the electronic (Zhou et al., 2021) and high-tech industries, jewellery (Burat et al., 2019), and the chemical industry (Li et al., 2021b). In the last few decades, especially due to technological advances, gold has become increasingly used in metal finishing, metallurgy, electroplating, and electronic industry (Hubenova et al., 2023). There is a rise in gold demand due to its wide range of applications and thus requires additional resources to recover gold. Gold extraction processes, both in mining operations and industrial activities like metal plating, electronics manufacturing, and chemical processing, often result in gold loss through inefficient recovery methods, accidental spills, and insufficient treatment of wastewater. Recovering gold from waste resources presents an opportunity to meet this demand sustainably. However, the concentration of gold in tailings and industrial effluents is typically extremely low, requiring advanced techniques for the recovery of trace gold concentrations. Therefore, developing advanced technologies is essential to effectively recover gold from these sources while minimizing environmental impact and maximizing resource efficiency.

Recovering and removing valuable metals from gold mining tailings and wastewater streams is necessary due to their high economic value and because of their effect on human health and environmental concerns (Aghaei et al., 2017). Various extraction methodologies were used for the detection and recovery of gold from solid and liquid media such as solid-phase (Aghaei et al., 2017), liquid-liquid (Wang et al., 2021a) and magnetic solid-phase extraction (MSPE) (Aghaei et al., 2017). Moreover, coprecipitation (Soylak and Tuzen, 2008), adsorption (Nasrollahzadeh et al., 2021), cloud point extraction methods (Oya et al., 2014), and ion exchange (Alguacil, 2018) are a few of the most frequently employed techniques. Among them, adsorbents have been extensively used for gold reclamation in the last few decades. The modern development of adsorbents for extraction of gold includes porous aromatic frameworks (PAFs) (Li et al., 2021b), metal-organic frameworks (MOFs) (Li et al.,

* Corresponding author.
E-mail address: elsa.antunes1@jcu.edu.au (E. Antunes).

https://doi.org/10.1016/j.jclepro.2024.142317
Received 20 December 2023; Received in revised form 15 April 2024; Accepted 21 April 2024
Available online 22 April 2024

Nomenclature and expressions

ANN	Artificial neural network
AC	Adsorption capacity
Eα	Activation energy
BBD	Box-Behnken design
CCD	Central composite design
KAS	Kissinger-Akahira-Sunose
F	Freundlich
A	Frequency factor
FCC	Fixed Carbon Content
L	Langmuir
R_L	Langmuir separation factor
ICP-AES	Inductively coupled plasma-atomic emission spectroscopy
IPD	Intraparticle diffusion
M	Moisture
MWCNTs	Multi-walled carbon nanotubes
OFW	Ozawa-Flynn-Wall
PFO	Pseudo-first order
PSO	Pseudo-second order
RSM	Response surface methodology
RMSE	Root means square error
SEM	Scanning electron microscopy
EDS	Energy dispersive X-ray spectroscopy
SSA	Salp swarm algorithm
T	Temkin
XPS	X-ray photoelectron spectroscopy
V	Volatile
α_0	Constant in quadratic equation
α_i	Linear constant in quadratic equation
α_{ii}	Quadratic terms in quadratic equation
α_{ij}	Interaction terms in quadratic equation
Qexp	Experimental adsorption capacity
Qpred	Predicted adsorption capacity

2021b), covalent organic frameworks (COFs) (Qian et al., 2020), and porous organic polymers (POPs) (Hong et al., 2020). However, these adsorbents are highly expensive and cannot be used commercially for the large-scale operation.

One of the most widely used and traditional adsorbents is activated carbon (AC) (Yu et al., 2017), while more recent and emerging ones include carbon materials (Zhou et al., 2021), ion-imprinted sorbents (Dobrzynska et al., 2018), carbon nanotubes (CNTs) (Pang and Yung, 2014), graphene oxide (Yang et al., 2017), nanomaterials (Koyanaka et al., 2005), bio-sorbents like chitosan, bacterial biomass, algal, mesoporous silica (Ebrahimzadeh et al., 2010), resins (Losev et al., 2018), and polymeric materials (Can et al., 2016). However, slow adsorption rate, reduced adsorption capacity, and most importantly, unable to be recycled for having poor stability are the main reasons to neglect the use of these adsorbents. Most remediation procedures are costly, complicated, and cause secondary contamination (Zhou et al., 2021).

Activated carbon (Soleimani and Kaghazchi, 2008), carbon nanotubes (Birtane et al., 2022) and biochar (Zhou et al., 2021) are some examples of adsorbents that have recently been explored for gold (Au) adsorption. Multi-walled carbon nanotubes (MWCNTs) exhibited 62.3 mg/g Au (III) adsorption capacity from water samples (Shaheen et al., 2015). Moreover, a cyanide-gold aqueous solution containing a concentration of 0.01 g/L at 20 °C temperature exhibited 52.5% Au (I) adsorption by MWCNTs (Alguacil, 2018). In addition, corn straw biochar showed 98% gold adsorption efficiency from gold-iodized solutions (Zhou et al., 2021). The economic benefit of biomass adsorbents is higher than using other adsorbing materials. For this reason, biomass-derived biochar has obtained potential importance as an adsorbent. It can be synthesized from the pyrolysis of different types of biomasses, such as agricultural waste, sawdust, orange peel, tea waste, wood chips, and sewage sludge (Antunes et al., 2018). For example, it can be used for gold recovery in wastewater (Li et al., 2021a). Furthermore, environmental pollution may be reduced by avoiding the post-treatment pollution of commercial adsorbents.

Extraction of gold particles from waste streams especially gold mines that generate tonnes of tailing offers an exciting opportunity for resource recovery. In addition, the usage of biochar makes the gold extraction process a sustainable and cost-effective method. Biochar has been proven a promising candidate for gold adsorption due to its high surface area, porous structure, and abundance of functional groups like hydroxyl and carboxyl which may provide adequate sites for gold adsorption (Zhou et al., 2021). The application of biochar for gold adsorption and optimization of adsorption kinetics has been less explored and demands more comprehensive studies to understand gold adsorption on biochar. Therefore, this study investigates the production of a high-quality biochar from the pyrolysis of ironbark (IB) for effective and economical gold recovery from aqueous solutions. Ironbark sawdust biochar was employed for gold adsorption and optimized the adsorption process with different *agitation speeds* (rpm), *reaction times* (minutes), and *gold concentrations* (ppm) using Response Surface Methodology (RSM) and Artificial Neural Networks (ANN) and Salp Swarm Algorithm (SSA) models. A comparison was drawn to estimate the accuracy of the models. Later, gold adsorption behaviour was estimated using kinetics and isotherm analysis. The biochar was characterized using various techniques like X-ray diffraction (XRD), X-ray photoelectron spectroscopy (XPS), Brunauer-Emmett-Teller (BET), Transmission Electron Microscopy (TEM) and Scanning Electron Microscopy with Energy Dispersive X-ray Spectroscopy (SEM-EDS) to confirm the presence of gold particles and their existing states, and subsequently, gold adsorption mechanism on biochar was speculated. This study will add significance to the application of biochar for gold recovery from aqueous solutions and advance the understanding of process optimization to achieve maximum results.

2. Experimental

Materials: Gold chloride ($AuCl_3$) was ordered from Sigma-Aldrich (CAS No: 13,453-07-1; Source: MKCQ0083; Purity: 99%).

Preliminary experiment: To select the best biochar for Au adsorption, preliminary tests have been done on three different biochars: algae, spent coffee grounds, and ironbark for gold adsorption from an aqueous solution (Table S1). Among them, IB biochar showed the highest adsorption capacity. Thus, IB biochar has been used for investigating gold adsorption by biochar.

2.1. Synthesis of IB biochar adsorbent

Ironbark (IB) biomass was collected from a nearby shop in Townsville, Queensland, Australia. Firstly, IB biomass was placed for drying in a oven at 105 °C to eliminate moisture. Secondly, around 10 g of biomass waste was used to prepare biochar. IB biomass was pyrolyzed at 500 °C in an N_2 atmosphere in a typical fixed bed electrical tube (quartz) furnace-Termolab. In addition, the heating rate was 10 °C/min, and the residence period was 30 min. Finally, IB biochar was used to reclaim gold from aqueous media with known gold concentration.

2.2. Characterization of biomass/biochar

Approximately 20 mg of IB biomass was tested for thermogravimetric analysis (TGA). The thermogravimetric experiment of IB biomass

was carried out using the 'Discovery TA/SDT650' analyser. Experiments were performed in a nitrogen atmosphere (50 ml/min N_2 flow rate), where temperature ranged from 25 to 1000 °C with 5, 10 and 15 °C/min heating rates. The TGA curves were created by plotting a residual mass percentage vs. temperature. Later, the TGA curve was utilized to calculate the moisture content (%) and volatile matter (%) as well as ash content. After collecting the data from the TGA curve, the fixed carbon content (%) was calculated using equation (1):

$$Fixed\ carbon\ content\ (\%) = 100\% - (Moisture\ \% + Volatile\ \% + Ash\ \%) \quad (1)$$

Pyrolysis kinetics and thermodynamic formulae used in this experiment are described in detail in the supplementary material. Enthalpy (ΔH), entropy (ΔS), and Gibbs free energy (ΔG) were calculated as these are important for understanding the pyrolysis mechanism.

The Brunauer-Emmett-Teller (BET) model was utilized to determine the surface area. The N_2 physisorption isotherms and specific surface area of IB biochar were investigated at 196 °C utilizing a Micromeritics Tristar 3020 apparatus. Before analysis, samples were degassed at 300 °C for 6 h under vacuum. The Barrett-Joyner-Halenda (BJH) isotherm was utilized to calculate mesoporous diameter and volume.

The X-ray diffraction (XRD) equipment was utilized to find out the structural characteristics, and crystallinity of biochar before and after gold adsorption. Biochar was collected after adsorption experiments from the liquid phase using a syringe, filtered by a membrane (0.22 μm) and then dried at 105 °C, and then analysis was done by XRD at room temperature. It has been noted that the sample was run in a low-volume sample holder with a narrower slit (0.2 mm instead of 1.0 mm). A Bruker D2 Phaser X-ray Powder Diffractometer was utilized with scan mode setting continuous position sensitive detector (PSD) fast. The scan was done between 10 and 90° and the XRD condition was followed at 1sec/step with an increment size of 0.02 or step size.

Scanning electron microscopy (SEM) and EDS (Energy dispersive x-ray spectroscopy) were applied to find out the morphological properties of biochar. Biochar (BC) samples were dispersed in water and drop cast on a silicon wafer for SEM-EDS analysis. A Scanning Electron Microscope (SU5000, X-Max, OXFORD instrument, Hitachi) was used for the analysis and evaluated at EC = 115 nA, Vac = 5.0 kV, and WD = 7.5 mm.

Transmission Electron Microscopy (TEM) was employed to image the ironbark biochar nanostructure before and after gold adsorption. Samples were suspended in 100% ethanol, sonicated for 5 min, and then drop-cast onto 300-mesh, lacey carbon-coated copper grids. Grids were air-dried and left overnight in a 60 °C oven to remove hydrocarbons. Samples were imaged at 200 kV on a JEOL JEM-2100 TEM mounted with a TVIPS F416 4K CCD camera.

X-ray photoelectron spectroscopy (XPS) was performed to inspect the physiochemical state of the gold-loaded biochar. For XPS measurements, a Kratos Axis Supra equipped with a monochromatic AI Kα X-ray and a helium lamp was utilized. The C 1s peak calibrated the binding energy at 284.6 eV. XPS peaks were deconvoluted, and distinct gold ions were identified on IB biochar by CASA XPS software.

2.3. Adsorption experiment of IB biochar

Before and after adsorption, the gold content in the aqueous solution was measured by ICP-AES. The adsorption capability (AC) and % of gold removal of the IB biochar are expressed in equations (2) and (3).

$$\boldsymbol{q_e} = \frac{(\boldsymbol{C_e} - \boldsymbol{C_0}) \times \boldsymbol{V}}{\boldsymbol{M}} \quad (2)$$

$$\%\ \boldsymbol{of\ Gold\ removal}\ (\boldsymbol{R}) = \frac{\boldsymbol{C_0} - \boldsymbol{C_e}}{\boldsymbol{C_0}} \times \mathbf{100} \quad (3)$$

where R represents % gold removal efficiency, q_e stands for the equilibrium adsorption capacity of the absorbent, the starting and final (equilibrium) concentrations are represented by C_0 and C_e (mg/L) accordingly, V (L) is the volume, and M (g) is the quantity of the IB biochar.

2.4. Adsorption kinetics and isotherms

Gold adsorption kinetics were performed by adding 0.04 g IB biochar to 400 mL of gold chloride ($AuCl_3$) solution containing an initial gold content of 100 mg/L and stirring the mixture at 400 rpm for varying contact times (from 10 min to 22 h). Approximately, 10 mL of sample was collected with a syringe, filtered through a 0.22 μm membrane, and finally evaluated by ICP-AES. Several mathematical models (Table 1) were compared to fit the experimental data.

To measure the effect of the primary content of gold in the aqueous solutions, firstly, various concentrations of 25, 50, 100, 150, and 200 mg/L gold aqueous solutions were prepared by adding properly measured gold chloride in double-distilled water. In each initial concentration, 0.010 g of IB biochar was added to 100 mL of gold solution agitated for 17 h at 400 rpm at ambient temperature (24 °C). After 17 h about 10 mL of each sample was filtered fluid through a 0.22 μm membrane for further analyses. Several isotherm models mentioned in Table 1 were used to evaluate the experimental results. R_L was next selected to assess the material's affinity for Au (III) at various starting concentrations (Chen et al., 2022).

2.5. Gold adsorption capacity experimental design and modelling

2.5.1. Response surface methodology (RSM) design

RSM is a dynamic mathematical and statistical method that performs polynomial and quadratic integration using a few independent variables. RSM generates a model that most accurately depicts the whole process (Mahmad et al., 2023). Moreover, this method may be used to create and optimize a variety of experimental circumstances in a wide range of scientific and engineering projects. Based on the input variables of the model, the output variables may be forecasted (Samadi-Maybodi and Nikou, 2020). For example, RSM has been utilized to examine the data on eliminating contaminants from the environment's waterways (Yang et al., 2020).

The experiment in which the IB biochar adsorbed Au (III) from the liquid phase was conducted by RSM using the Design-Expert software, and in this experiment, the central composite design (CCD) was utilized. Input parameters were *agitation speed* (rpm), *contact time* (rpm), and *gold*

Table 1
Summary of reported adsorption kinetics and isotherms models.

Experiment	Model type	Mathematical expressions	
		Linear	Non-linear
Adsorption kinetics	Pseudo-first order (PFO)	$ln(q_e - q_t) = ln\ q_e - k_1 t$	$q_t = q_e(1 - e^{k_1 t})$
	Pseudo-second order (PSO)	$\frac{t}{q_t} = \frac{1}{k_2 q_e^2} + \frac{1}{q_e}$	$q_t = \frac{k_2 q_e^2 t}{1 + k_2 q_e t}$
	Intraparticle diffusion	$q_t = \frac{1}{\beta}\ln(\alpha\beta) + \frac{1}{\beta} lnt$	$q_t = K_3\sqrt{t} + C$
	Elovich	$q_t = \beta \ln(T) + \beta \ln(\alpha)$	$q_t = \frac{1}{\beta}\ln(1 + \alpha\beta T)$
Adsorption isotherms	Freundlich	$log\ q_e = log\ K_F + \frac{1}{n} log\ C_e$	$q_e = K_F C_e^{\frac{1}{n}}$
	Langmuir	$\frac{1}{q_e} = \frac{1}{K_L q_m}.\frac{1}{C_e} + \frac{1}{q_m}$ $*R_L = \frac{1}{1 + K_L C_0}$	$q_e = \frac{K_L q_m C_e}{1 + K_L C_e}$
	Temkin	$q_e = \frac{RT}{b}\ln K_T + \frac{RT}{b} ln\ C_e$	$q_e = \frac{RT}{b}\ln(K_T C_e)$

Where, $*R_L$ = Equilibrium factor; $R_L = 0$: adsorption is irreversible, $0 < R_L < 1$: adsorption is favourable; $R_L = 1$: linear nature of adsorption; $R_L > 1$: adsorption is unfavourable.

concentration (ppm). Variables that were found impactful were optimized to maximize gold adsorption by IB biochar. This was done with a combination of the CCD model and the RSM. For the three selected parameters, 15 runs were considered for designing CCD to optimize the maximum gold adsorption capacity of IB biochar from an aqueous solution.

The lower, middle, and upper levels for the parameters are presented in Table 2 and results were analysed to find a quadratic equation (4) for modelling the adsorption process.

$$Q = \alpha_0 + \sum_{i=1}^{k} \alpha_i X_i + \sum_{i=1}^{k} \alpha_{ii} X_{ii}^2 + \sum_{i=1}^{k-1} \sum_{j=2}^{k} \alpha_{ij} X_i X_j + \varepsilon \quad i \neq j \tag{4}$$

where Q is the predicted adsorption capacity, inputs are X_i and X_j, the number of independent parameters is denoted by k (here k = 3), and the random error is ε. The analysis of variance (ANOVA) was applied to evaluate the efficacy of the model at the 95% confidence level.

The response surface methodology laboratory experiment was done with 15 experiments with the above-mentioned actual values. The RSM was used to predict the response with different factorial values.

2.5.2. Artificial neural network modelling

Artificial neural networks (ANN) have shown promise as a tool for simulation, prediction, and modelling because of their apparent ease of use (Esfe et al., 2023). ANN has the potential for stronger non-linear generalisation and can handle a larger number of input variables (Jiang et al., 2022a). Moreover, the adsorption kinetics are complicated, but ANN can be used to forecast the adsorption profile (Alardhi et al., 2023). Adsorption systems could be better described by ANN models than by generic models (Prakash et al., 2008). However, standard mathematical models may be used to describe removal processes, but doing so is time-consuming and costly due to the need for a large number of trials (Samadi-Maybodi and Nikou, 2020). Moreover, it is laborious to use conventional mathematical models to model and enhance the elimination processes (Can et al., 2016). Wastewater treatment processes are notoriously complex since they are affected by a wide range of operational factors and elimination methods (Samadi-Maybodi and Nikou, 2020). The benefits of ANN include their capability to learn complex relationships without needing the information of the model structure, their shorter development time compared to traditional mathematical models, and the fact that only a small number of trials are needed to predict the degree of non-linearity (Prakash et al., 2008). For example, it has been shown ANN to model the recovery of *sarafloxacin* from water solutions. Recently, the usage of ANN to model wastewater remediation processes has been investigated (Jawad et al., 2021).

As described earlier, ANN is a powerful tool to separate non-linear connections and has been extensively implemented over the last few decades to tackle engineering design challenges. The right efficiency of ANN anticipated the accurate selection of weights and biases. Thus, by selecting an appropriate hybrid ANN, these weights may be improved, potentially increasing the suitability and productivity of ANN (Soleimani et al., 2023). The Salp Swarm Algorithm (SSA) is a meta-heuristic algorithm inspired by nature that may solve a variety of optimization issues by replicating its behaviour in nature. Mirjalili proposed the SSA, a population-based optimization technique (Mirjalili et al., 2017), which is one of the artificial intelligence optimization methods. In SSA, people are classified as either leaders or followers depending on where they are in the chain. The chain begins with a leader, and the chain serves as a direction for the followers' motions (Abualigah et al., 2019).

To increase the performance of ANN, the weights and biases were optimized using SSA. In this article, the hybrid of ANN and SSA (ANN-SSA) was used to model adsorption capacity. The Python programming language was utilized to create ANN-SSA. Different Python packages were used for calculations and graphs. The applied ANN in this work has a 3:5:1 topology which is shown in Fig. 1 (a). The *speed* (A), *time* (B), and *concentration* (C) are the input layers whereas the output layer has one neuron to calculate adsorption capacity. In this modelling for hidden and output layers tansig and purelin were used as transfer functions.

The applied method to optimize the applied ANN is shown in Fig. 1 (b). A Python code for SSA was written based on EvoloPy which contains optimization techniques (https://github.com/7ossam81/EvoloPy). The correlation coefficient (R^2) and RMSE were utilized to compare both models as follows by equations (5) and (6).

$$R^2 = 1 - \frac{\sum_{i=1}^{n} \left(Q_{exp,i} - Q_{pred,i}\right)^2}{\sum_{i=1}^{n} \left(Q_{exp,i} - \overline{Q_{pred,i}}\right)^2} \tag{5}$$

$$RMSE = \sqrt{\frac{\sum_{i=1}^{n} \left(Q_{pred,i} - Q_{exp,i}\right)^2}{n}} \tag{6}$$

In summary, one of the key benefits of response surface methodology (RSM) is that it enables the collection of a significant amount of information from an extremely limited number of experiments. Models and graphical depictions can analyze the primary effects of factors and their interactions on the response. Conversely, neural networks possess several benefits, such as the necessity of less formal statistical study, the capability to completely identify complicated nonlinear relationships between dependent and independent variables, the ability to detect any probable interactions among variables that can be predicted, and the availability of multiple learning algorithms (Shafizadeh et al., 2023).

3. Results and discussion

3.1. Proximate and TGA/DTG analysis of IB biochar

The proximate analysis of IB biochar is provided in Table S2. Fig. 2 (a) shows the thermogravimetric analysis (TGA) graph of IB biochar at heating rates of 10 °C/min under a nitrogen environment to understand the mass loss pattern of biomass. Based on the findings, ironbark sawdust biomass TGA may be broadly broken down into three distinct steps. The first stage involved removing moisture up to 211 °C (about 10%), which was then followed by devolatilization. Moreover, at temperatures ranging from 211 to 508 °C, a variety of volatile compounds (74.61%) were produced during the degradation process of various hemicelluloses, cellulose, and some parts of lignin, which is called the second stage (Dada et al., 2022). The breakdown of various residual lignins, with a solid residue of 4.40%, determined the third stage, which ranged from 509 to 808 °C. The highest weight loss occurred at around 380 °C with 0.8 wt %/°C as shown by the derivative thermogravimetric (DTG) curve.

It was observed that the highest temperatures of the next stage in the DTG curve moved upward to greater temperatures as the heating rate increased. This finding supports the hypothesis that the thermal decomposition process is slowed down when the energy rate is increased (Ceylan et al., 2014). The final step, which is known as the passive pyrolysis stage, is characterised by the gradual breakdown of the lignin component and the production of biochar. This stage takes place after the active pyrolysis stage (Sharma et al., 2023). The thermogravimetric analysis (TGA) graph provided insights into the kinetic parameters of thermal degradation and the reaction mechanism of IB biomass (Nawaz

Table 2
Actual and coded levels of the selected independent variables.

Factor	Unit	Factor Code	Coded and actual levels		
			−1	0	+1
Speed	rpm	A	200	400	600
Time	min	B	30	60	90
Au concentration	ppm	C	50	100	150

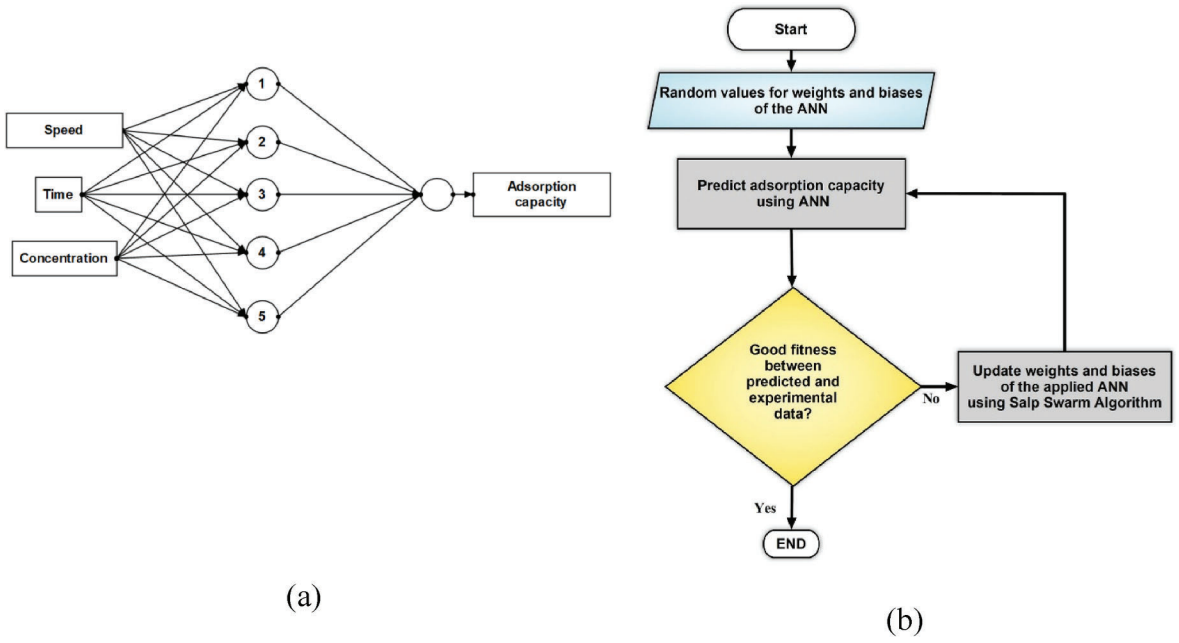

Fig. 1. (a) 3-5-1 topology structure in ANN architecture, (b) flowchart of ANN training process using SSA.

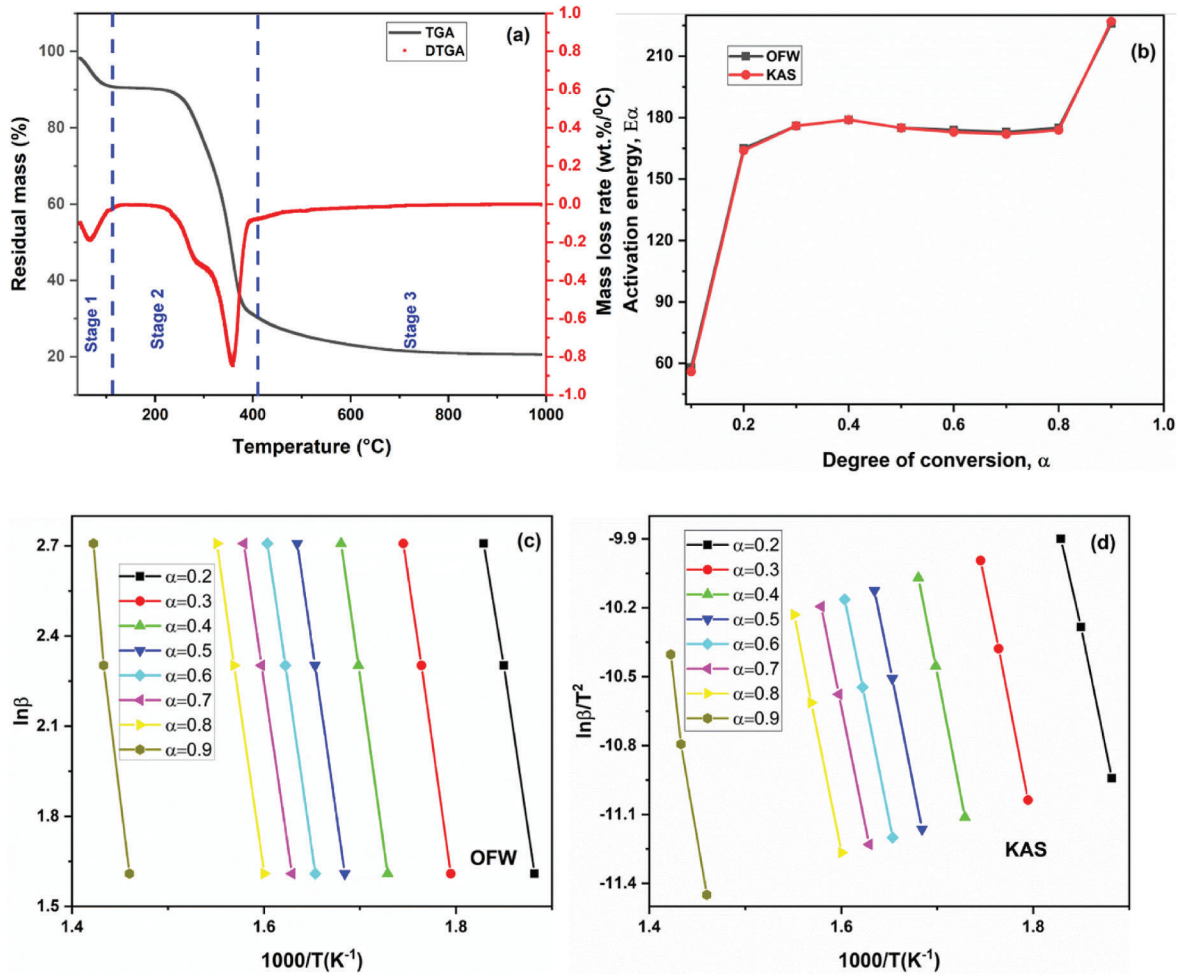

Fig. 2. (a) TGA and DTGA analysis of IB biomass to understand the thermal decomposition behaviour at 10 °C/min (b) Changes of activation energy while pyrolysis of IB biomass (c) Kinetic isoconversional plots graphs analysed from OFW and (d) KAS methods for IB biomass.

et al., 2021). This also revealed the activation energy at different stages throughout the time of the conversion process (Hu et al., 2016).

3.2. The pyrolysis kinetics and thermodynamics of ironbark biochar

3.2.1. Pyrolysis kinetics

Kinetic parameters including frequency factor (A) and activation energy (Eα) were analysed using the Kissinger-Akahira-Sunose (KAS) and Ozawa-Flynn-Wall (OFW) models and are provided in Table S4. The KAS technique projected an average activation energy (Eav) of 165.4 kJ/mol for the IB biomass, while the OFW method predicted 166.88 kJ/mol. The result also demonstrated a slight similarity with the literature on the Eucalyptus wood sawdust (Sharma et al., 2023). The high value of the fitting parameter ($R^2 > 0.99$) for both methods indicated the high precision of the data presented in Table S4.

The changes in activation energy (Eα) during the pyrolysis of biomass are shown in Fig. 2 (b). The calculated frequency factor (A) values varied between 1.08E+14 and 9.74E+15 min^{-1}, as determined by the KAS and the OFW techniques (Table S4). The low pre-exponential factors also suggested surface response, but the high pre-exponential factors suggested the development of the preferable activating complex, which likely limits displacement compared to the primary breakdown (Yuan et al., 2017).

Kinetic isothermal graphs with activation energies ranging from 0.2 to 0.9 obtained from OFW and KAS methods for pyrolysis of IB biomass at three different temperatures are shown in Fig. 2 (c-d). As the thermal conversion method is complex, a multi-step process cannot be represented using a single activation energy (Qu et al., 2023). The time dependence of the transformation processes is therefore oversimplified as a result of the application of this method, which offers a straightforward approach to the estimation of the activation energy by basing it on the peak temperature. This process is dependent on temperature and is quite difficult. Modelling and simulation of IB biomass thermal behaviour have shown results in excellent agreement with experimental data. Over the whole conversion range, the kinetic analysis, KAS, and OFW approach all produced similar Eα values.

Thermodynamic studies of IB biomass pyrolysis are also crucial to find out the pyrolysis mechanism and investigate the suitability of the overall pyrolysis technology. The activation energy which has been calculated from the KAS method was utilized to calculate enthalpy, entropy, and Gibbs free energy as shown in the supplementary data provided in Table S3. The endothermic nature of the pyrolysis process was demonstrated by the positive value of $\Delta H = 161.05$ kJ/mol, as presented in Table S3. The results showed that with increasing conversion, changes in Eα and both ΔH and ΔG increase, demonstrating that pyrolysis is endothermic and the thermodynamic efficiency decreases with increasing conversion (Qu et al., 2023). Table S3 also included the Gibbs free energy changes (ΔG), with an average value of 148.25 kJ/mol. The Gibbs free energy mostly represented the complete energy increment. While in the decomposed reactions, a progressive ΔG was found as the degree of conversion increased (Yuan et al., 2017).

3.3. Gold adsorption capacity by IB biochar

3.3.1. Investigation of the impact of contact time on Au adsorption

The investigation of the effect of contact time on the adsorption rate is shown in Table 3. The adsorption kinetics of IB biochar were studied for 10–1320 min. The findings of the experiments indicated that gold adsorption rate by IB biochar was initially fast, then slow, before reaching equilibrium. This finding also showed that with an increase in the contact period, biochar reached its maximum adsorption capacity, which was 858 mg/g. While beginning the adsorption, the surface of the adsorbent has a high number of adsorption sites that are able to attach gold, which in turn causes the adsorption capacity to considerably increase (Ukanwa et al., 2019). Because the number of attachable sites reduces as the process proceeds and the concentration of gold in the solution drops, the rate at which adsorption may occur gradually becomes more difficult to achieve (Rapo and Tonk, 2021). When all of the attachment sites on the surface of the adsorbent have been taken up, the adsorption process has reached a state of equilibrium.

Table 3
Gold adsorption kinetic parameters derived by using different kinetic models.

Kinetic Models		
	q_e, exp (mg/g)	858
Pseudo-first order (PFO)	q_m (mg/g)	706
	K_1 (min^{-1})	0.0027
	R^2	0.99
Pseudo-second order (PSO)	q_m (mg/g)	769
	K_2 (g ($min^{-1}mg^{-1}$))	0.000013
	R^2	0.95
Intra-particle diffusion (IPD)	q_m (mg/g)	949.23
	k_{diff}	23.39
	R^2	0.96
Elovich	q_m (mg/g)	1080
	b	0.0068
	R^2	0.92

Four kinetics models have been used to fit the experimental data, as described in Table 3. The Pseudo-first order (PFO) kinetic model exhibited the highest R^2 value of 0.99 and the second order kinetic model showed an R^2 value of 0.95. According to the PFO kinetic model, the adsorption process relies heavily on monolayer adsorption (physical adsorption). Physisorption is the major adsorption mechanism so the PFO kinetic model fits well with the experimental data for Au (III) adsorption by IB biochar. However, the Pseudo-second-order (PSO) kinetic model ($R^2 = 0.95$) which mainly represents chemisorption also fits the experimental data well. Multiple variables, including mass transfer and internal diffusion, can dominate the adsorption process. This finding suggests that the Au adsorption onto biochar starts with surface adsorption followed by internal pore diffusion (Zhou et al., 2021). Diffusion in adsorption systems is governed by several different processes (Antunes et al., 2018). The mechanism and rate-controlling processes of diffusion are illustrated using intraparticle diffusion models. Intraparticle diffusion (IPD), was utilized to better characterise the adsorption of Au (III). R^2 value for IPD of 0.96 was calculated. Table 3 shows that IPD is the second-best fit for the experimental data. The IPD model has three adsorption stages: surface diffusion, pore diffusion, and adsorption of gold on the biochar pores which is the slowest stage (Antunes, E. et al., 2017).

3.3.2. Impact of initial concentration on Au adsorption

The investigation of the effect of initial concentration on the Au adsorption is provided in Table 4, increasing the gold concentration increased the adsorption capacity. The adsorption isotherms of IB biochar were studied with Au (III) ranging from 25 to 200 mg/L. The maximum experimental adsorption capacity of IB biochar for Au (III) was 858 mg/g. It was observed that IB biochar can efficiently recover

Table 4
Gold adsorption isothermal parameters calculated by using different theoretical models.

Isotherm Models		
	q_e, exp (mg/g)	551
Langmuir	q_m (mg/g)	625
	K_L (L/mg)	0.0376
	R^2	0.98
Freundlich	q_m (mg/g)	623
	n	2.80
	K_F	92.84
	R^2	0.77
	q_m (mg/g)	479
Temkin	K_t (g/L)	7.27
	B	267.76
	R^2	0.98

gold from aqueous solutions from different concentrations.

To further investigate the adsorption process, three isotherm models mentioned in Table 1 were employed to match the experimental outcomes. The data revealed that the correlation coefficient (R^2) order was 0.9844 (Langmuir) > 0.9804 (Temkin) > 0.7709 (Freundlich). As a result, the Langmuir model is best suited. Langmuir adsorption is a type of single-layer adsorption that is supposed to be adsorbed on a homogenous medium. Moreover, the Langmuir model suggested that the ironbark biochar contained a uniform type of active sites, and the adsorption of gold (Au) followed the monolayer adsorption. Furthermore, it suggested that there was no interaction between Au particles. Thus, gold adsorption by IB biochar followed the monolayer adsorption as indicated by the Langmuir isotherms, which are observed in several literatures (Zhou et al., 2021). Moreover, $R_L < 1$ confirmed that the adsorption was favourable.

The different adsorbents for gold (Au) in the literature are listed in Table 5 and the adsorption capacity obtained by IB biochar (this study) was three times higher than the biochar adsorption capacity mentioned in the literature because IB biochar has a high S_{BET} surface area which is 493.8 m^2/g. For example, boron-nitrogen-doped biochar showed 246.96 mg/g adsorption capacity which is less than IB biochar results (Wang et al., 2021b). As listed in Table 5, it can be concluded that IB biochar showed the highest adsorption capacity for removing gold from aqueous solutions.

3.4. Evaluation of the model for Au adsorption capacity

3.4.1. Response surface methodology analysis

The experimental and predicted results for RSM and ANN are presented in Table 6. In both models, the effects of *time*, *rotation speed*, and *initial concentration* were examined. The highest adsorption capacity was shown at 200 rpm, with a 150-ppm initial concentration in 30 min. The data also revealed that there was no exceptional variance between the actual and predicted values of adsorption capacity mentioned in Table 6. ANN showed more accurate adsorption capacity than RSM in comparison with the experimental values.

The statistical analysis of the RSM is presented in Table 7. According to the analysed ANOVA, the low p-value (=0.0002) reveals that the model is significant, and $R^2 = 0.99$ is in good agreement with the Adj. R-squared = 0.97. Therefore, the quadratic model (Eq. (7)) can be used for analysis of the experimental results.

$$\text{Adsorption capacity (mg/g)} = 242.62 - 7.34A + 10.67B + 37.87C + 4.70AB - 11.90AC - 15.29BC - 22.94A^2 + 10.54B^2 - 5.64C^2 \quad (7)$$

Where, A, B, and C are the coded values of *agitation speed*, *contact time*, and Au *initial concentration*, respectively.

The perturbation graph for each process factor is shown in Fig. S1. This graph indicates the various effects of *speed, time*, and *concentration* (independent variables) on adsorption capacity whereas the Au *concentration* is the more dominant parameter over other parameters. The adsorption capacity of IB biochar was increased with the increased concentration and time. On the other hand, *agitation speed* seems not to impact the biochar adsorption capacity.

The influence of the independent parameter's *agitation speed*, *time*, and *concentrations* on the adsorption capacity of IB biochar in 3D surface graphs is shown in Fig. 3. For all of these plots, the effect of two independent variables was shown in the response, whereas the third factor was constant at the middle level.

Fig. 3 (a) shows the mutual effects of *speed* and *time* on adsorption capacity at constant Au *concentration* (100 ppm). Around 80 min of *contact time* and *agitation speed* of 300 rpm, it has been revealed that the adsorption capacity with increased *speed* reached its highest value, but after reaching its peak, it decreased slightly with increasing *agitation speed*. Conversely, the adsorption capacity increased with increments of

Table 6
CCD with predicted and experimental responses.

Run	A Speed (rpm)	B Time (min)	C Conc. (ppm)	Adsorption capacity (mg/g)		
				Experimental	Predicted	
					RSM	ANN
1	200	90	50	203.4	203.4	202.1
2	200	30	150	294.3	291.0	292.9
3	200	90	150	271.3	272.3	269.9
4	200	60	100	224.9	227.0	229.5
5	200	30	50	160.5	160.8	161.3
6	400	60	100	252.7	242.6	247.1
7	400	60	150	269.6	274.8	275.0
8	400	60	50	199.2	199.1	200.0
9	400	30	100	235.8	242.4	239.6
10	400	90	100	265.3	263.8	266.3
11	600	30	150	244.3	243.1	245.6
12	600	90	50	219.8	221.9	221.0
13	600	90	150	244.8	243.2	244.9
14	600	30	50	162.8	160.6	164.6
15	600	60	100	209.3	212.3	210.0

Table 7
Analysis of variance results obtained from the RSM model.

Source	Sum of Squares	df	Mean Square	F-Value	p-value* (Prob > F)
Model	20973.66	9	2330.41	54.19	0.0002
A (Speed)	538.42	1	538.42	12.52	0.0166
B (Time)	1139.55	1	1139.55	26.50	0.0036
C (Au Conc.)	14342.69	1	14342.69	333.49	<0.0001
AB	176.70	1	176.70	4.11	0.0985
AC	1132.97	1	1132.97	26.34	0.0037
BC	1871.23	1	1871.23	43.51	0.0012
A^2	1352.96	1	1352.96	31.46	0.0025
B^2	285.63	1	285.63	6.64	0.0496
C^2	81.86	1	81.86	1.90	0.2262

Table 5
Reaction conditions, adsorption capacity and BET surface area of different adsorbents used for gold adsorption.

Adsorbents	Source of Gold	Reaction condition			Adsorption capacity (mg/g)	BET surface area (m^2/g)	Ref.
		Dosage (g/L)	Temperature (°C)	Reaction time (h)			
Carbon nanotube-cellulose based	River water	25	25	12	49.19	–	Birtane et al. (2022)
Purolite (MN202)	E-waste	1	19.85	6	259.45	–	Wojcik et al. (2023)
Coconut shell activated carbon	Cyanide leaching solution	1.25	25	3	1.79	–	Khosravi et al. (2017)
Raw date pits	Aqueous solution		24.85	1.5	78	285	Al-Saidi (2016)
B-N-doped walnut shell biochar	Aqueous solution		25	3	246.96	–	Wang et al. (2021b)
IB biochar	**Aqueous solution**	**0.1**	**24**	**22**	**858**	**493.8**	**This study**

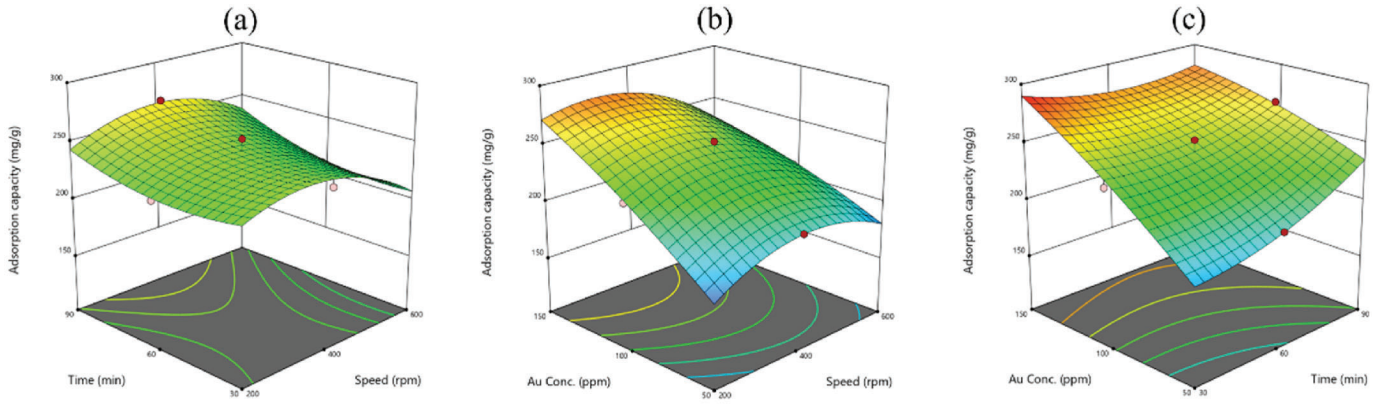

Fig. 3. 3D surface graphs of adsorption capacity of IB biochar response on the basis of (a) *agitation speed* (rpm) and *contact time* (min), (b) *agitation speed* (rpm) and initial Au *concentration* (ppm), and (c) *contact time* (min) and initial *Au concentration* (ppm).

contact time until it reached equilibrium at 80 min, which followed the adsorption kinetics process. This also indicated that *high speed* and low *contact time* showed the least adsorption capacity.

Based on Fig. 3 (b), it has been assumed that when *time* is constant (60 min), with increasing *concentration*, adsorption capacity increases, which confirms the adsorption isotherm methods because of the increased electromotive force of mass transfer between the liquid and solid media. Moreover, with increasing *speed*, the adsorption capacity also decreased moderately at constant *time*.

Therefore, regarding Fig. 3 (c), it was established that the combined effect of *time* and *concentration* showed the actual surface of the effect on adsorption capacity. The plot revealed that the best range of application of adsorbent concentration could be within 150 mg/L with the possibility of a higher adsorption capacity of 294.38 mg/g at a lower *contact time* of 30 min. Similarly, an *agitation speed* of 200 rpm is identified as the best, but it has been confirmed that *speed* has less effect on the adsorption capacity.

3.4.2. Analysis of artificial neural network (ANN)

Using the optimized weights and biases values using SSA, the performance of the ANN was better than RSM to represent the experimental data. The optimal values for weights and biases are presented in Table 8. Herein, the sum of square errors was minimised by the optimized 26 variables (number of weights and biases).

Equation (8) presents the matrix version of the adsorption capacity equation, which is based on weights and biases. In this equation, $[W]_{1\times5}$ is the output of the hidden layer (weights), $[q]_{5\times1}$ is the conversion matrix of the output, and [b] is the output biases of the hidden layer accordingly.

$$\textit{Adsorption capacity}\left(\frac{mg}{g}\right) = \left([W]_{1\times5}\times[q]^{T}_{5\times1} + [b] + 1\right)\times\frac{(294.376 - 160.575)}{2} + 160.575 \tag{8}$$

where,

$$[W]_{1\times5} = [W2\,]$$

$$[q]_{5\times1} = \begin{bmatrix} \frac{2}{1+e^{-2p_1}} - 1 \\ \frac{2}{1+e^{-2p_2}} - 1 \\ \frac{2}{1+e^{-2p_3}} - 1 \\ \frac{2}{1+e^{-2p_4}} - 1 \\ \frac{2}{1+e^{-2p_5}} - 1 \end{bmatrix}$$

$$[b] = [B2]$$

In addition, the p_i matrix is calculated following the below equation.

$$\begin{bmatrix} p_1 \\ p_2 \\ p_3 \\ p_4 \\ p_5 \end{bmatrix} = [W1]\times\begin{bmatrix} 2\frac{(Speed\ (rpm) - 200)}{(600-200)} - 1 \\ 2\frac{(Time\ (min) - 30)}{(90-30)} - 1 \\ 2\frac{(Au\ Concentration\ (ppm) - 50)}{(150-50)} - 1 \end{bmatrix} + [B1]$$

3.4.3. Artificial neural network (ANN) comparison with RSM

For more accuracy, statistical measures of quality of fit of RSM and ANN-SSA were investigated. The statistical results for the efficiency of RSM and ANN-SSA are shown in Table 9. Both RSM and ANN-SSA models have a good capability to predict adsorption capacity. Root means square error (RMSE) of the applied ANN was lower than the RSM and the coefficient of correlation (R^2) for RSM and ANN models were 0.99 and 0.995, accordingly. Thus, the ANN-SSA root means square error (RMSE) was 2.71 that is lower than the RMSE (3.786) for RSM. These results show that ANN-SSA can better predict the gold adsorption by ironbark biochar.

Table 8
Optimum weights and biases for ANN-SSA model for 3-5-1 topology.

Neuron	Input (3)-Hidden Layer (5)				Neuron	Hidden Layer (5)-Output (1)	
	Weights (W1)			Biases (B1)		Weights (W2)	Biases (B2)
1	0.530554289	−0.454880164	−0.814009769	0.001126256	1	−0.167551334	−0.72378114
2	0.093105045	−0.664201393	−0.881322869	−0.848214286	2	−0.470208586	
3	0.761212398	−0.39411436	0.108350219	−0.680194773	3	−0.999999925	
4	0.015946021	−0.992188798	0.293133989	−1	4	0.815435089	
5	−0.861165	−0.191765278	−0.387386782	−0.920954686	5	−0.99597998	

Table 9
Statistical measures of quality of fit of RSM and ANN-SSA.

Error function	RSM	ANN-SSA
Correlation coefficient (R^2)	0.990	0.995
Root means square error (RMSE)	3.786	2.712

The statistical data presented show evidence that the predictions generated by the artificial neural network (ANN) model closely align with the experimental values, exhibiting little error function. Hence, the current investigation validated the significance and superior performance of the ANN-SSA model in comparison to response surface methodology in forecasting experimental data.

3.5. Characterization of gold-loaded biochar (before and after adsorption)

The specific surface area and pore diameter are key factors in the adsorption of gold ions that cannot be overlooked. The ironbark biochar achieved S_{BET} specific surface area of 493.79 m^2/g, pore size of 2.17 nm, and pore volume of 0.167 cm^3/g. The high surface area could be explained by the high lignin content of IB biochar (Dada et al., 2021). Moreover, the physical and chemical changes of biochar can occur due to the release of volatile organic compounds during pyrolysis which can also increase the surface area of the biochar material (Antunes et al., 2017a,b). Fig. 4(a) contains information on the N_2 adsorption-desorption isotherm of ironbark biochar, which is a type IV isotherm that is characteristic of a mesoporous structure. A rounded knee indicates the approximate location of monolayer formation and hysteresis indicates capillary condensation in meso and macropores (Qiu et al., 2018). This high specific surface area indicates a large number of active sites available for adsorption and chemical interactions, making biochar highly effective for adsorbing gold ions from aqueous solutions. The mesoporous structure of the biochar may provide adequate space for gold ions to penetrate and interact with the biochar surface. The collective textural properties may enhance the biochar's adsorption capacity and efficiency for gold ions. Fig. 4 (b) depicts the results of N_2 adsorption-desorption studies in terms of pore diameters (BJH).

The crystallinity and structure of biochar were determined using XRD. The Au (III) adsorption on the biochar was confirmed by XRD. Fig. 5 showed the XRD spectra of ironbark biochar before and after Au (III) adsorption. Before adsorption, JCPDS indexed card no.50–0926 revealed that IB biochar XRD morphology displayed sharp diffraction peaks at 2θ of 22.8°, 29.4°, and 39.50°, following that biochar consisted primarily of amorphous carbon (Mo et al., 2021). After the adsorption of Au onto the ironbark biochar (IB-BC), the intensity of a big band on the surface that corresponds to the amorphous carbon was greatly reduced. AuNPs were observed sharply at 2θ values of 38.10° (111), 44.13° (200),

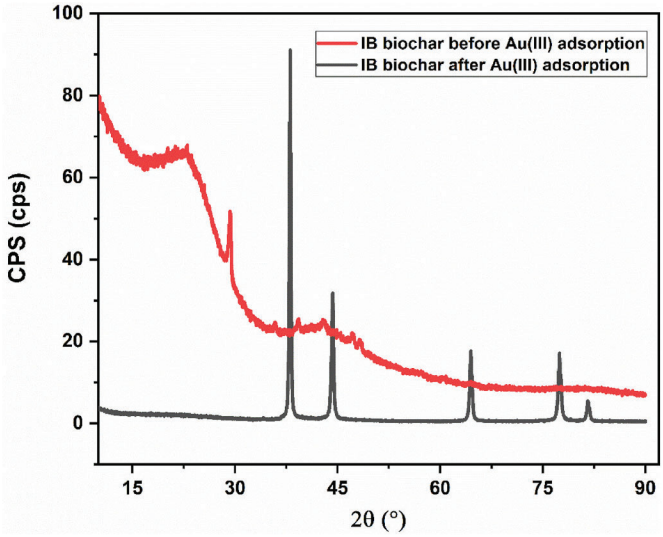

Fig. 5. XRD spectra of ironbark-derived biochar pyrolyzed at 500 °C before and after Au (III) adsorption from aqueous solution.

64.43° (220) and 77.32° (311), respectively, after Au adsorption by IB biochar. The represented XRD peaks manifested the pure AuNPs by comparing the graph patterns with the JCPDS database number 00-004-0784 (Ganash et al., 2022).

SEM coupled with EDS was applied to study the macrostructural properties and gold adsorption on IB biochar. SEM was also used to find out the size and properties of ironbark biochar before and after gold adsorption. Fig. 6 (1: a-d) presents the SEM images at different magnifications of IB biochar pyrolyzed at 500 °C showing the morphology and pore structure characteristics. The IB biochar exhibited uneven, rigid, both regular and irregular rougher surfaces, some channels, small regular particles, flat surfaces, and its elements were heterogeneous (Singh et al., 2021) and similar to those reported for modified eucalyptus bark biochar (Yusuff et al., 2022). The data presented in this figure indicates that the biochar particles exhibit an irregular shape, and further analysis reveals that gold nanoparticles (AuNPs) are formed and deposited on the surface of the biochar.

The similar morphology of IB biochar is shown in Fig. 6 (2: e-h) the EDS images and distribution of gold after IB biochar adsorption from the aqueous solution. EDS images confirmed that the white/red spots are gold nanoparticles, and clearly showed the agglomeration of gold on IB biochar surfaces. Not surprisingly, carbon was predominant in the IB

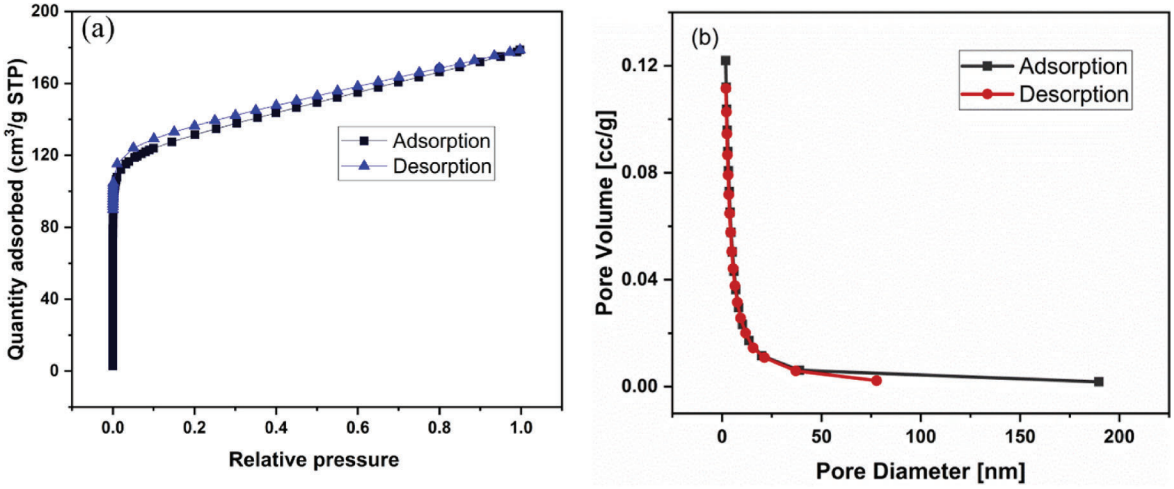

Fig. 4. N_2 Adsorption-desorption **(a)** by BET; **(b)** pore size distributions by BJH of Ironbark biochar.

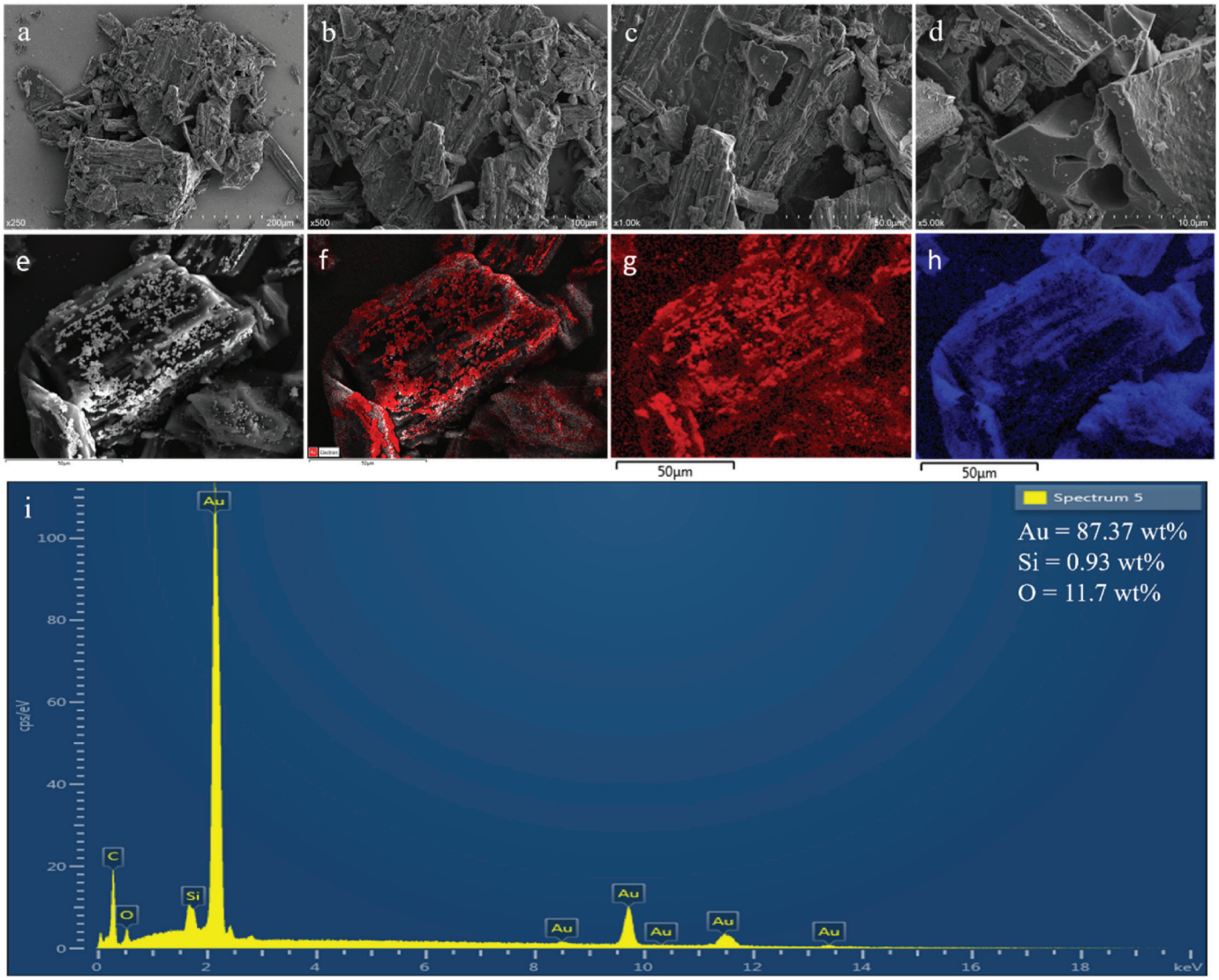

Fig. 6. (1) SEM pictures of IB biochar produced at 500 °C before Au (III) adsorption (a-d) at different magnifications (250, 500, 1000, 5000); (2) SEM-EDS pictures of IB biochar produced at 500 °C after Au adsorption (e: backscatter image: gold; f: EDS layered image; g: gold, h: Carbon) and EDS mapping graph (i) indicating the elemental quantification on biochar after Au adsorption.

biochar, and the elemental composition also showed the presence of Au approximately 87.37 wt%, which anchored on the surfaces of biochar.

Transmission electron microscopy (TEM) showed in Fig. 7confirmed the layered amorphous carbon matrix, and stacked sheets with porous structure (20 nm) of ironbark biochar before gold adsorption in Fig. 7(a and b). The TEM images also showed the lattice fringe of IB biochar before adsorption (Zhou et al., 2020). An experiment with Pecan shell biochar TEM images verified that gold nanoparticles are either aggregated on the biochar surface or aligned on the edges of the sheet layer in the biochar (Uchimiya et al., 2017). Therefore, after gold adsorption by ironbark biochar in Fig. 7(c and d) revealed that the gold nanoparticles (AuNPs) with spherical shapes with 4–18 nm sizes formed and aggregated on the IB biochar in different areas.

X-ray photoelectron spectroscopy (XPS) was employed to find out the oxidation states of biochar surfaces and the elemental content of gold-loaded biochar. Peaks of different chemical states were displayed in survey spectra of the XPS before and after Au adsorption in Fig. 8 (a) and **(b)** the Au 4f orbital signal of the absorbed IB biochar. In addition, after adsorption, it was visible in the Au survey spectra as gold-loaded biochar. All the peaks are assigned to various orbitals but are dominated by Au $4f_{5/2}$ and Au $4f_{7/2}$. These peaks confirmed the zero-valent metallic Au^0 state in the Au 4f spectrum which is similar to the $4f_{5/2}$ and $4f_{7/2}$ peaks at 85.14 and 84.06 eV binding energy (BEs), respectively (Deokar and Ingale, 2023).

Moreover, Fig. 8(b) showed that the Au 4f peak occurs at 85.14 eV, with the Au $4f_{7/2}$ component perhaps representing Au^0 with an area of 41.78% and the second highest Au^1 with 35.56%, respectively area covered in those oxidation states (de la Torre-Miranda et al., 2023). The Au 4f spectra on the gold-loaded biochar exhibit the expected chemistry of gold Au^0 (Deokar and Ingale, 2023). The chemical transformation of Au (III) into Au^0 was accomplished. The lower BE (83.99 eV) is attributed to Au^0, whereas the higher BE (84.5 eV) is attributed to Au (I) (85.14 eV) with more bulk gold (Shah et al., 2023). As a result, the XPS spectra at 83.78 eV showed no distinct signal for Au (III). This strongly suggests that a gold-related chemical reaction takes place during the removal of gold by IB biochar (Niu et al., 2023). The Au adsorption of the IB biochar is governed by both physisorption and chemical adsorption, as shown by the aforementioned investigation.

Fig. 8(c and d) shows the after-gold adsorption of the C 1s and O 1s spectra and Fig. S2 (a and b) depicts the C 1s and O 1s spectra both before and after the gold adsorption process. C spectra can show that the C signal is comprised of different chemical functionalized groups (Niu

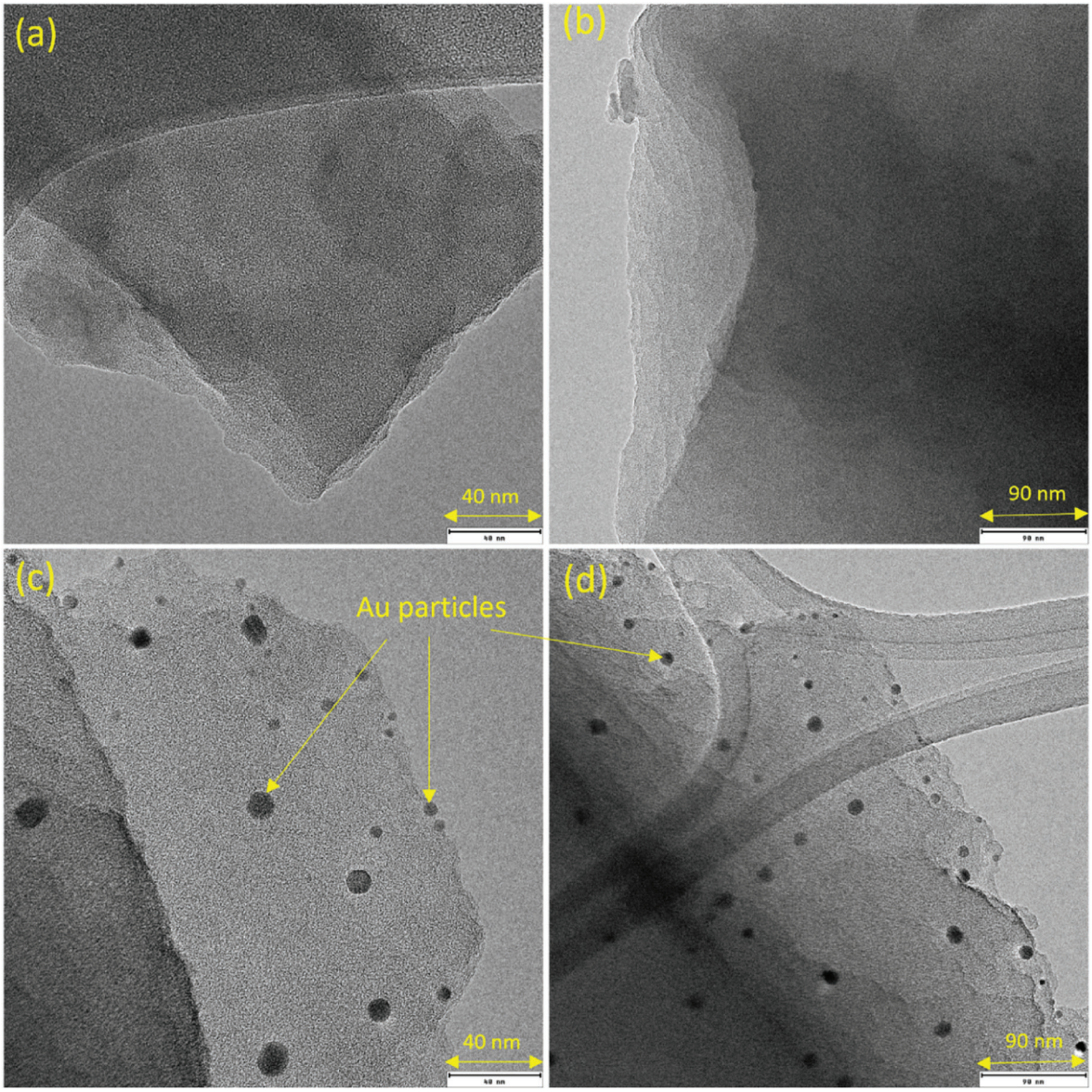

Fig. 7. TEM images (a) and (b) of biochar before adsorption and (c) and (d) after gold adsorption.

et al., 2023). Before adsorption takes place, the peaks of the C spectrum are observed at 284.77 eV while after adsorption move to 285.59 eV. Because of this, it may be concluded that the adsorption system modifies not only the charge and electron cloud density in the vicinity of the C atom but also the chemical state of the atom itself (Niu et al., 2023). Moreover, this also confirmed that it has a connection among the shifting chemical states of carbon atoms and the behaviour of adsorption, which is implied by the previous statement. As with C spectra, the only change that can be observed in O 1s spectra is also a shift in the binding energy.

4. Mechanism of gold adsorption on IB biochar

Analysis by techniques like XRD, SEM, TEM and EDS verified the existence of elements including O, C, and Au on biochar after adsorption. The XPS analysis also showed the presence of oxidation states of functional groups whereas the XRD analysis revealed the conversion of Au ions into Au metal. From the kinetic model, the PFO model has been the main model for gold removal, which confirmed the physisorption is the main mechanism for gold adsorption by IB biochar. The mechanism by which metal ions are attached to biochar may be categorized into several processes including ion exchange, precipitation, complexation, physical adsorption, and electrostatic interaction (Fig. 9). The porous nature of the biochar, as shown by SEM and BET measurements, makes it plausible that Au ions might follow the physisorption (physical precipitation) of the IB biochar utilizing van der Waals forces. In addition, the mesoporous structure illustrated in ironbark biochar BET (Fig. 4) provided a high number of adsorption sites. Thus, the biochar's surface may act as an adsorption site for Au ions, or the ions may seep into the biochar's pores.

However, depending on the pore size and surface, physical adsorption may have a relatively low binding strength. Water molecules may serve as an agent between the biochar surface and the gold (Xiong et al., 2021). Prior to filling the pores of the biochar with gold ions, gold molecules might form a complex with water molecules. This would make the biochar more effective at adsorbing gold from the solution. The biochar contains elements such as carbon (C), calcium (Ca), and chlorine (Cl) to interact with Au ions, as observed by SEM-EDS before gold adsorption (Fig. S3). These results suggest that electrostatic attraction between Au and outer surface charged biochar could be

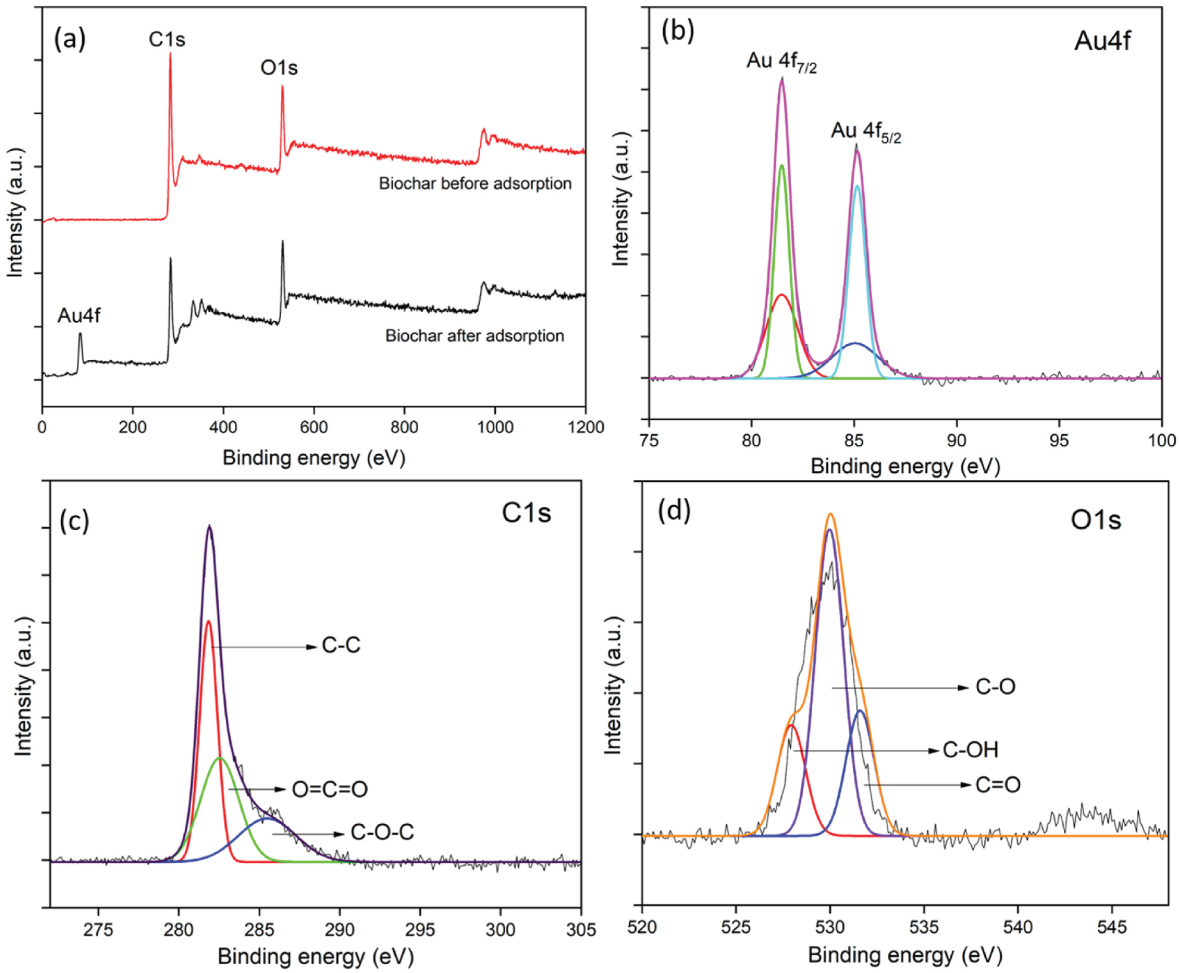

Fig. 8. (a) XPS survey scan spectra of IB biochar before and after gold adsorption (b) XPS measurement of gold-loaded IB biochar at Au 4f orbital; (c) XPS graph of C 1s and (d) O 1s orbital spectra after the gold adsorption by IB biochar.

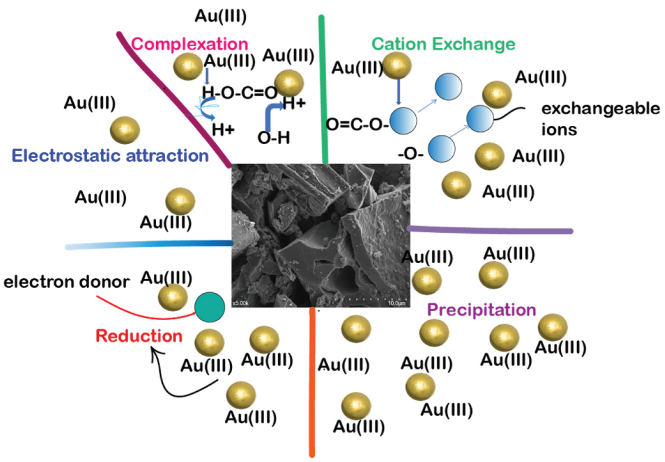

Fig. 9. Possible mechanism of gold adsorption by ironbark biochar.

another mechanism for Au removal. The pH of the solution plays a critical role in the adsorption of gold due to its impact on the surface chemistry of both gold ions and biochar. Biochar surfaces may carry positive charges at low pH due to the protonation of functional groups and negative charges at high pH due to deprotonation. At low pH, the positive charge enhances the adsorption of gold ions onto the biochar surface. The electrostatic attraction between the positively charged biochar and gold ions may promote adsorption.

XPS analysis revealed that the C=C and C=O rings could be involved in the adsorption process, suggesting that surface complexation and metal-π interactions may represent possible mechanisms. Interestingly, biochar can form various chemical oxidation states of gold nanoparticles by acting as a reductant (Uchimiya et al., 2017). Therefore, oxidation states which are confirmed by XPS analysis assist for the reduction of gold (III) ions to metallic gold (Ahmad et al., 2023). Moreover, the O-aliphatic and O-aromatic bonds which are shown in the XPS graph of biochar may assist strong hydrogen bonding due to the surface charges of IB biochar, and gold nanoparticles contributed to the reduction mechanism (Al-Saidi, 2016). Similarly, the existence of metal Au nanoparticles in the biochar was verified by XRD and TEM image analysis, indicating that reduction occurred concurrently with Au adsorption.

5. Significance of the study

This research showcases the utilization of biomass-derived biochar for gold adsorption presents a compelling advancement with multiple advantages. By harnessing renewable biomass resources, the study maximizes resource utilization and offers cost-effective alternatives to conventional adsorbents and catalysts. The study successfully showed that biochar could be highly efficient in removing gold particles and can be applied in the gold mining industry to extract gold from tailings or other gold-contaminated wastewater. On the other hand, spent biochar could be a cost-effective catalyst to produce value-added products like

phenols which could serve as precursor compounds to produce high-energy-density hydrocarbons. Therefore, it could be stated that this work underscores the potential of biochar as a sustainable and multi-functional material, offering environmental, economic, and social benefits in various industrial sectors.

The spent biochar could be regenerated using several methods like chemical, thermal, electrochemical or a combination of these methods. Chemical regeneration is the most common method applied for biochar regeneration, which involves the utilization of solvents and chemical reagents to desorb the adsorbate like Au. There are numerous studies that showed biochar regeneration utilized for the adsorption of heavy metals. Therefore, similar methods with certain modifications can be applied for Au-biochar regeneration. For example, a study utilized a variety of solvents like HNO_3, EDTA and NaOH for biochar regeneration used for Pb adsorbent (Jiang et al., 2022b). The results showed that NaOH-regenerated biochar achieved better recycling performance compared to HNO_3 and EDTA. The biochar regenerated by NaOH maintained nearly 84% desorption efficiency whereas HNO_3 and EDTA-treated biochar could maintain only 20% of desorption efficiency. Similarly, the implementation of surface modification techniques may enhance biochar stability and gold adsorption capacity. Functionalization with substances like oxygen-containing groups (e.g., hydroxyl, carboxyl) through oxidation processes can increase surface polarity and reactivity, promoting stronger interactions with gold ions.

6. Conclusions

This study investigated that the highest Au adsorption capacity of IB biochar was 858 mg/g at 1320 min. The adsorption of gold by IB biochar was confirmed by XRD, XPS, SEM-EDS and TEM. Furthermore, the dependence of adsorption capacity on components was analysed by using Response Surface Methodology (RSM) and Artificial Neural Networks (ANN) and Salp Swarm Algorithm (SSA) to investigate the adsorption patterns of IB biochar with three input variables (*agitation speed*, *contact time*, and initial *Au concentration*). The ANN-SSA technique was used to construct the data-driven model and a 3:5:1 topology ANN-SSA was used. Gold adsorption capacity data was better predicted by the ANN-SSA than by the RSM, according to statistical comparisons, and the ANN-SSA shows with the best topology. The RSM method was able to get the explicit regression equation and provide a convincing defence of the interaction between parameters. This research demonstrated that IB biochar is a sustainable adsorbent for the recovery of Au (III) from aqueous solutions.

CRediT authorship contribution statement

Mahmuda Akter Mele: Writing – original draft, Methodology, Formal analysis, Data curation. **Ravinder Kumar:** Writing – review & editing. **Tewodros Kassa Dada:** Validation, Methodology. **Amir Heydari:** Software. **Elsa Antunes:** Writing – review & editing, Supervision, Project administration, Funding acquisition, Conceptualization.

Declaration of competing interest

The authors declare the following financial interests/personal relationships which may be considered as potential competing interests:

The authors declare that they have no known competing financial interests or personal relationships that could have appeared to influence the work reported in this paper.

Data availability

Data will be made available on request.

Acknowledgements

Authors are grateful to James Cook University and Research Training Program Scholarship (RTP).

Appendix A. Supplementary data

Supplementary data to this article can be found online at https://doi.org/10.1016/j.jclepro.2024.142317.

References

Abualigah, L., Shehab, M., Alshinwan, M., Alabool, H., 2019. Salp swarm algorithm: a comprehensive survey. Neural Comput. Appl. 32 (15), 11195–11215.
Aghaei, E., Alorro, R., Encila, A., Yoo, K., 2017. Magnetic adsorbents for the recovery of precious metals from Leach solutions and wastewater. Metals 7 (12).
Ahmad, M., Shah, T., Tariq, M.R., Zhang, L., Lyu, Y., Iqbal, W., Naik, M.u.-d., Khosla, A., Zhang, Q., Zhang, B., 2023. Recent trends in material design and preparation with structure-activity relationship for gold recovery from E-waste: a review. J. Clean. Prod. 426.
Al-Saidi, H.M., 2016. The fast recovery of gold(III) ions from aqueous solutions using raw date pits: kinetic, thermodynamic and equilibrium studies. J. Saudi Chem. Soc. 20 (6), 615–624.
Alardhi, S.M., Fiyadh, S.S., Salman, A.D., Adelikhah, M., 2023. Prediction of methyl orange dye (MO) adsorption using activated carbon with an artificial neural network optimization modeling. Heliyon 9 (1), e12888.
Alguacil, F., 2018. Adsorption of gold(I) and gold(III) using multiwalled carbon nanotubes. Appl. Sci. 8 (11).
Antunes, E., Schumann, J., Brodie, G., Jacob, M.V., Schneider, P.A., 2017a. Biochar produced from biosolids using a single-mode microwave: characterisation and its potential for phosphorus removal. J. Environ. Manag. 196, 119–126.
Antunes, Elsa, Jacob, M.V., Brodie, G., Schneider, P.A., 2018. Microwave pyrolysis of sewage biosolids: dielectric properties, microwave susceptor role and its impact on biochar properties. J. Anal. Appl. Pyrol. 129, 93–100.
Antunes, E., Jacob, M.V., Brodie, G., Schneider, P.A., 2017b. Silver removal from aqueous solution by biochar produced from biosolids via microwave pyrolysis. J. Environ. Manag. 203, 264–272.
Bansal, S.A., Kumar, V., Karimi, J., Singh, A.P., Kumar, S., 2020. Role of gold nanoparticles in advanced biomedical applications. Nanoscale Adv. 2 (9), 3764–3787.
Birtane, H., Urucu, O.A., Yıldız, N., Çiğil, A.B., Kahraman, M.V., 2022. Statistical optimization and selective uptake of Au(III) from aqueous solution using carbon nanotube-cellulose based adsorbent. Mater. Today Commun. 30.
Burat, F., Basturkcu, H., Ozer, M., 2019. Gold&silver recovery from jewelry waste with combination of physical and physicochemical methods. Waste Manag. 89, 10–20.
Can, M., Doğan, M., İmamoğlu, M., Arslan, M., 2016. III) uptake by triazine polyamine polymers: mechanism, kinetic and equilibrium studies. React. Funct. Polym. 109, 151–161.
Carabineiro, S.A.C., 2019. Supported gold nanoparticles as catalysts for the oxidation of alcohols and alkanes. Front. Chem. 7, 702.
Ceylan, S., Topcu, Y., Ceylan, Z., 2014. Thermal behaviour and kinetics of alga Polysiphonia elongata biomass during pyrolysis. Bioresour. Technol. 171, 193–198.
Chen, Y., Li, Z., Ding, R., Liu, T., Zhao, H., Zhang, X., 2022. Construction of porphyrin and viologen-linked cationic porous organic polymer for efficient and selective gold recovery. J. Hazard Mater. 426, 128073.
Dada, T.K., Islam, M.A., Duan, A.X., Antunes, E., 2022. Catalytic co-pyrolysis of ironbark and waste cooking oil using X-strontium/Y-zeolite (X= Ni, Cu, Zn, Ag, and Fe). J. Energy Inst. 104, 89–97.
Dada, T.K., Sheehan, M., Murugavelh, S., Antunes, E., 2021. A review on catalytic pyrolysis for high-quality bio-oil production from biomass. Biomass Conversion and Biorefinery 13 (4), 2595–2614.
de la Torre-Miranda, N., Reilly, L., Eloy, P., Poleunis, C., Hermans, S., 2023. Thiol functionalized activated carbon for gold thiosulfate recovery, an analysis of the interactions between gold and sulfur functions. Carbon 204, 254–267.
Deokar, G.K., Ingale, A.G., 2023. Exploring effective catalytic degradation of organic pollutant dyes using environment benign, green engineered gold nanoparticles. Inorg. Chem. Commun. 151.
Dobrzynska, J., Dabrowska, M., Olchowski, R., Dobrowolski, R., 2018. An ion-imprinted thiocyanato-functionalized mesoporous silica for preconcentration of gold(III) prior to its quantitation by slurry sampling graphite furnace AAS. Mikrochim. Acta 185 (12), 564.
Ebrahimzadeh, H., Tavassoli, N., Amini, M.M., Fazaeli, Y., Abedi, H., 2010. Determination of very low levels of gold and palladium in wastewater and soil samples by atomic absorption after preconcentration on modified MCM-48 and MCM-41 silica. Talanta 81 (4–5), 1183–1188.
Esfe, M.H., Esmaily, R., Khabaz, M.K., Alizadeh, A.a., Pirmoradian, M., Rahmanian, A., Toghraie, D., 2023. A novel integrated model to improve the dynamic viscosity of MWCNT-Al2O3 (40:60)/Oil 5W50 hybrid nano-lubricant using artificial neural networks (ANNs). Tribol. Int. 178.
Ganash, A., Alshammari, S., Ganash, E., 2022. Development of a novel electrochemical sensor based on gold nanoparticle-modified carbon-paste electrode for the detection of Congo red dye. Molecules 28 (1).

Hong, Y., Thirion, D., Subramanian, S., Yoo, M., Choi, H., Kim, H.Y., Stoddart, J.F., Yavuz, C.T., 2020. Precious metal recovery from electronic waste by a porous porphyrin polymer. Proc Natl Acad Sci U S A 117 (28), 16174–16180.
Hu, M., Chen, Z., Wang, S., Guo, D., Ma, C., Zhou, Y., Chen, J., Laghari, M., Fazal, S., Xiao, B., Zhang, B., Ma, S., 2016. Thermogravimetric kinetics of lignocellulosic biomass slow pyrolysis using distributed activation energy model, Fraser–Suzuki deconvolution, and iso-conversional method. Energy Convers. Manag. 118, 1–11.
Hubenova, Y., Chorbadzhiyska, E., Kostov, K.L., Mitov, M., 2023. Efficient gold recovery by microbial electrochemical technologies. Bioelectrochemistry 149, 108311.
Jawad, J., Hawari, A.H., Javaid Zaidi, S., 2021. Artificial neural network modeling of wastewater treatment and desalination using membrane processes: a review. Chem. Eng. J. 419.
Jiang, H., Zahmatkesh, S., Yang, J., Wang, H., Wang, C., 2022a. Ultrasound-enhanced catalytic degradation of simulated dye wastewater using waste printed circuit boards: catalytic performance and artificial neuron network-based simulation. Environ. Monit. Assess. 195 (1), 144.
Jiang, S., Yan, L., Wang, R., Li, G., Rao, P., Ju, M., Jian, L., Guo, X., Che, L., 2022b. Recyclable nitrogen-doped biochar via low-temperature pyrolysis for enhanced lead (II) removal. Chemosphere 286 (Pt 1), 131666.
Khosravi, R., Azizi, A., Ghaedrahmati, R., Gupta, V.K., Agarwal, S., 2017. Adsorption of gold from cyanide leaching solution onto activated carbon originating from coconut shell—optimization, kinetics and equilibrium studies. J. Ind. Eng. Chem. 54, 464–471.
Koyanaka, H., Takeuchi, K., Loong, C.K., 2005. Gold recovery from parts-per-trillion-level aqueous solutions by a nanostructured Mn2O3 adsorbent. Separation and Purification Technology 43 (1), 9–15.
Li, Haoyu, Peng, J., Long, H., Li, S., Zhang, L., 2021a. Cleaner process: efficacy of chlorine in the recycling of gold from gold-containing tailings. J. Clean. Prod. 287.
Li, Xue-Jing, Cui, W.-R., Jiang, W., Yan, R.-H., Liang, R.-P., Qiu, J.-D., 2021b. Bi-functional natural polymers for highly efficient adsorption and reduction of gold. Chem. Eng. J. 422.
Losev, V.N., Elsufiev, E.V., Buyko, O.V., Trofimchuk, A.K., Horda, R.V., Legenchuk, O.V., 2018. Extraction of precious metals from industrial solutions by the pine (Pinus sylvestris) sawdust-based biosorbent modified with thiourea groups. Hydrometallurgy 176, 118–128.
Mahmad, A., Zango, Z.U., Noh, T.U., Usman, F., Aldaghri, O.A., Ibnaouf, K.H., Shaharun, M.S., 2023. Response surface methodology and artificial neural network for prediction and validation of bisphenol a adsorption onto zeolite imidazole framework. Groundwater for Sustainable Development 21.
Mirjalili, S., Gandomi, A.H., Mirjalili, S.Z., Saremi, S., Faris, H., Mirjalili, S.M., 2017. Salp Swarm Algorithm: a bio-inspired optimizer for engineering design problems. Adv. Eng. Software 114, 163–191.
Mo, Z., Shi, Q., Zeng, H., Lu, Z., Bi, J., Zhang, H., Rinklebe, J., Lima, E.C., Rashid, A., Shahab, A., 2021. Efficient removal of Cd(II) from aqueous environment by potassium permanganate-modified eucalyptus biochar. Biomass Conversion and Biorefinery.
Nasrollahzadeh, M., Sajjadi, M., Iravani, S., Varma, R.S., 2021. Green-synthesized nanocatalysts and nanomaterials for water treatment: current challenges and future perspectives. J. Hazard Mater. 401, 123401.
Nawaz, A., Mishra, R.K., Sabbarwal, S., Kumar, P., 2021. Studies of physicochemical characterization and pyrolysis behavior of low-value waste biomass using Thermogravimetric analyzer: evaluation of kinetic and thermodynamic parameters. Bioresour. Technol. Rep. 16.
Niu, H., Yang, H., Tong, L., Kamali, A.R., 2023. The adsorption characteristics and performance of gold onto elemental carbon extracted from refractory carbonaceous gold concentrate. Colloids Surf. A Physicochem. Eng. Asp. 658.
Oya, A.U., Zeynep, Y.G., Sabahattin, D., Ece, K.Y., Adnan, A., 2014. A novel ligand for cloud point extraction to determine gold content in ore samples. Environ. Chem. Lett. 12 (3), 449–453.
Pang, S.-K., Yung, K.-C., 2014. Prerequisites for achieving gold adsorption by multiwalled carbon nanotubes in gold recovery. Chem. Eng. Sci. 107, 58–65.
Prakash, N., Manikandan, S.A., Govindarajan, L., Vijayagopal, V., 2008. Prediction of biosorption efficiency for the removal of copper(II) using artificial neural networks. J. Hazard Mater. 152 (3), 1268–1275.
Qian, H.L., Meng, F.L., Yang, C.X., Yan, X.P., 2020. Irreversible amide-linked covalent organic framework for selective and ultrafast gold recovery. Angew Chem. Int. Ed. Engl. 59 (40), 17607–17613.
Qiu, Z., Wang, Y., Bi, X., Zhou, T., Zhou, J., Zhao, J., Miao, Z., Yi, W., Fu, P., Zhuo, S., 2018. Biochar-based carbons with hierarchical micro-meso-macro porosity for high rate and long cycle life supercapacitors. J. Power Sources 376, 82–90.
Qu, J., Zhang, B., Tong, H., Liu, Y., Wang, S., Wei, S., Wang, L., Wang, Y., Zhang, Y., 2023. High-efficiency decontamination of Pb(II) and tetracycline in contaminated water using ball-milled magnetic bone derived biochar. J. Clean. Prod. 385.
Rapo, E., Tonk, S., 2021. Factors affecting synthetic dye adsorption; desorption studies: a review of results from the last five years (2017-2021). Molecules 26 (17).
Samadi-Maybodi, A., Nikou, M., 2020. Removal of sarafloxacin from aqueous solution by a magnetized metal-organic framework; Artificial neural network modeling. Polyhedron 179.
Shafizadeh, A., Shahbeik, H., Nadian, M.H., Gupta, V.K., Nizami, A.-S., Lam, S.S., Peng, W., Pan, J., Tabatabaei, M., Aghbashlo, M., 2023. Turning hazardous volatile matter compounds into fuel by catalytic steam reforming: an evolutionary machine learning approach. J. Clean. Prod. 413.
Shah, S.A., Hu, K.-J., Naveed, M., Lu, C., Hu, S., 2023. Synthesis and study of the quantum-confinement effect of gold-nanoclusters via optical properties protected by 2-phenylethanethiol ligand. Chem. Phys. Lett. 811.
Shaheen, H.A., Marwani, H.M., Soliman, E.M., 2015. Selective adsorption of gold ions from complex system using oxidized multi-walled carbon nanotubes. J. Mol. Liq. 212, 480–486.
Sharma, A., Aravind Kumar, A., Mohanty, B., Sawarkar, A.N., 2023. Critical insights into pyrolysis and co-pyrolysis of poplar and eucalyptus wood sawdust: physico-chemical characterization, kinetic triplets, reaction mechanism, and thermodynamic analysis. Renew. Energy 210, 321–334.
Singh, R., Dutta, R.K., Naik, D.V., Ray, A., Kanaujia, P.K., 2021. High surface area Eucalyptus wood biochar for the removal of phenol from petroleum refinery wastewater. Environmental Challenges 5.
Soleimani, M., Kaghazchi, T., 2008. Adsorption of gold ions from industrial wastewater using activated carbon derived from hard shell of apricot stones - an agricultural waste. Bioresour. Technol. 99 (13), 5374–5383.
Soleimani, S., Heydari, A., Fattahi, M., 2023. Swelling prediction of calcium alginate/cellulose nanocrystal hydrogels using response surface methodology and artificial neural network. Ind. Crop. Prod. 192.
Soylak, M., Tuzen, M., 2008. Coprecipitation of gold(III), palladium(II) and lead(II) for their flame atomic absorption spectrometric determinations. J. Hazard Mater. 152 (2), 656–661.
Uchimiya, M., Pignatello, J.J., White, J.C., Hu, S.L., Ferreira, P.J., 2017. Surface interactions between gold nanoparticles and biochar. Sci. Rep. 7 (1), 5027.
Ukanwa, K., Patchigolla, K., Sakrabani, R., Anthony, E., Mandavgane, S., 2019. A review of chemicals to produce activated carbon from agricultural waste biomass. Sustainability 11 (22).
Wang, Min, Wang, Q., Wang, J., Liu, R., Zhang, G., Yang, Y., 2021a. Homogenous liquid–liquid extraction of Au(III) from acidic medium by ionic liquid thermomorphic systems. ACS Sustain. Chem. Eng. 9 (13), 4894–4902.
Wang, Zejuan, Xu, X., Ma, S., Wang, H., Zhao, H., Wang, Y., Tong, S., Su, Z., Wang, W., Bai, J., 2021b. The superior adsorption capacity of boron-nitrogen co-doping walnut shell biochar powder for Au(III), Pt(IV), and Pd(II). J. Environ. Chem. Eng. 9 (6).
Wojcik, G., Gorska-Parat, M., Hubicki, Z., Zinkowska, K., 2023. Selective recovery of gold from electronic waste by new efficient type of sorbent. Materials 16 (3).
Xiong, Q., Jiang, S., Fang, R., Chen, L., Liu, S., Liu, Y., Yin, S., Hou, H., Wu, X., 2021. An environmental-friendly approach to remove cyanide in gold smelting pulp by chlorination aided and corncob biochar: performance and mechanisms. J. Hazard Mater. 408, 124465.
Yang, J., Ma, C., Tao, J., Li, J., Du, K., Wei, Z., Chen, C., Wang, Z., Zhao, C., Ma, M., 2020. Optimization of polyvinylamine-modified nanocellulose for chlorpyrifos adsorption by central composite design. Carbohydr. Polym. 245, 116542.
Yang, L., Jia, F., Song, S., 2017. Recovery of [Au(CN) 2] − from gold cyanidation with graphene oxide as adsorbent. Separation and Purification Technology 186, 63–69.
Yu, H., Zi, F., Hu, X., Nie, Y., Chen, Y., Cheng, H., 2017. Adsorption of gold from thiosulfate solutions with chemically modified activated carbon. Adsorpt. Sci. Technol. 36 (1–2), 408–428.
Yuan, X., He, T., Cao, H., Yuan, Q., 2017. Cattle manure pyrolysis process: kinetic and thermodynamic analysis with isoconversional methods. Renew. Energy 107, 489–496.
Yusuff, A.S., Lala, M.A., Thompson-Yusuff, K.A., Babatunde, E.O., 2022. ZnCl2-modified eucalyptus bark biochar as adsorbent: preparation, characterization and its application in adsorption of Cr(VI) from aqueous solutions. South African Journal of Chemical Engineering 42, 138–145.
Zhou, W., Liang, H., Lu, Y., Xu, H., Jiao, Y., 2021. Adsorption of gold from waste mobile phones by biochar and activated carbon in gold iodized solution. Waste Manag. 120, 530–537.
Zhou, Y., Liu, S., Liu, Y., Tan, X., Liu, N., Wen, J., 2020. Efficient removal 17-estradiol by graphene-like magnetic sawdust biochar: preparation condition and adsorption mechanism. Int. J. Environ. Res. Publ. Health 17 (22).